Environmental Science
Advances

ROYAL SOCIETY
OF CHEMISTRY

PAPER

View Article Online
View Journal | View Issue

Check for updates

Cite this: *Environ. Sci.: Adv.*, 2026, **5**, 206

Received 24th September 2025
Accepted 10th November 2025

DOI: 10.1039/d5va00337g

rsc.li/esadvances

A non-contact *in situ* approach for detecting fluorescent microplastic particles in flowing water using fluorescence spectroscopy

Nico Merck, * Jonas Otto, Martin Schaeper and Nils Damaschke

Microplastic (MP) pollution poses increasing risks to aquatic ecosystems and, through the food chain, also to humans. Current detection methods rely on elaborate laboratory procedures such as Raman or FTIR spectroscopy, which involve extensive sample preparation, complex and costly instrumentation, and long analysis times, limiting their suitability for *in situ* monitoring. Reliable environmental assessment, however, requires continuous detection of MPs directly in flowing water. This study investigates the feasibility of combining fluorescence spectroscopy and interferometric particle imaging (IPI), the latter relying on particle scattering of coherent light and the detection of interference patterns, for detecting and characterising individual fluorescent MP particles under flow conditions. Each technique was initially evaluated separately to establish its feasibility. Polypropylene (PP) particles with and without incorporated fluorescent dyes were prepared, suspended in a flow-through cuvette, and illuminated by a laser diode at 445 nm. Fluorescence spectra and defocused particle images were recorded. Spectral analysis focused on emission maxima, full width at half maximum, and intensity ratios, while IPI provided information on particle type and size. Fluorescence spectroscopy enabled a clear separation between two main particle classes (yellow/green *vs.* orange/pink) based on spectral peak positions. Additional differentiation was achievable through intensity ratios and numerical clustering (PCA and subsequent LDA). Pure PP served as a negative control, confirming that fluorescence originates from dyes rather than the polymer matrix. However, absolute fluorescence intensities proved unreliable due to variations in particle size, dye type, and orientation. IPI images enabled the differentiation of air bubbles from PP particles and indicated the potential for particle sizing. Together, these findings demonstrate the feasibility of both fluorescence-based classification and IPI analysis under flow conditions, outlining a pathway towards simpler and more robust *in situ* monitoring of MPs in aquatic environments.

Environmental significance

Microplastic pollution is a growing environmental concern due to its persistence, ubiquity, and potential impacts on aquatic ecosystems and human health. A key challenge is the reliable detection and classification of microplastic particles in complex environmental matrices. Our study demonstrates that fluorescence spectroscopy enables the clear separation of polypropylene particles with different intrinsic fluorescent dyes, while interferometric particle imaging provides complementary information on particle size and material differentiation. This combined optical approach offers a robust pathway for non-destructive, real-time analysis of microplastics under flow conditions. By advancing particle characterisation methods, our findings contribute to the development of rapid monitoring strategies, supporting more accurate assessments of microplastic pollution and its ecological consequences.

1 Introduction

Microplastic (MP) pollution increasingly threatens marine habitats,[1–3] posing serious risks to aquatic organisms[4–6] and, *via* the food chain, also to humans.[7–9] MPs are small plastic particles defined as being less than 5 mm in size by the National Oceanic and Atmospheric Administration (NOAA), originating from primary sources such as microbeads in personal care products,[10–12] MP fibres from synthetic textiles[13,14] or from the degradation of larger plastic debris (secondary sources).[11,15]

Analysing MP sources, sinks, and concentrations remains challenging due to limited sampling possibilities and time-consuming laboratory analyses. Current methods for analysing MP concentrations (*e.g.* manual sampling, filtration, microscopic analysis, Fourier transform infrared (FTIR), or Raman spectroscopy) require an extensive sampling and filtering process that precedes the actual measurement.[16] It is

---

Institute of General Electrical Engineering, University of Rostock, Albert-Einstein-Straße 2, Rostock, 18059, Germany. E-mail: nico.merck@uni-rostock.de; Fax: +49 381 498 7081; Tel: +49 381 498 7053

not uncommon for several weeks to pass between sampling and the determination of sample composition.

To ensure reliable, long-term, and large-scale measurements, *in situ* solutions with continuous process sampling at adequate temporal resolution are required, enabling data collection at different locations with comparable results. As MP concentrations are frequently low, reliable detection is essential. Exhaustive particle detection is not mandatory, but accuracy is crucial: all detected particles must be conclusively identified as MPs.

1.1 Estimating particle concentrations

Concerning the investigation of MP pollution in marine habitats, the particle concentration is of particular interest. The technology of interferometric particle imaging (IPI) has proven to be a suitable approach for classifying and determining the size of particles in a flow based on the structures of scattered light.[17–19]

With IPI technology, the particles are illuminated by a laser beam and recorded in a deliberately defocused image plane.[17] Depending on the structure of the particles, *e.g.* as a bubble, crystal with facets or solid, they show different interference phenomena. Large bubbles exhibit a dense interference fringe pattern, whereas small bubbles have few interference fringes.[17,18] The speckle size is small for large solids and large for small solids.[20,21] The particle size in the image provides information about the particle distance from the camera. The larger the particle appears, the closer it is to the camera.[17]

In addition to classifying particles as a specific type based on their resulting structures, statistical parameters such as particle number concentration, volume concentration, and corresponding fluxes can also be determined, where the latter require knowledge of the flow velocity. It is further possible to determine the Sauter mean diameter d_{32} as a measure of active surface, since it relates the particle volume to its surface area and thus reflects the effective surface available for interfacial processes.[17]

Nowadays, particularly in marine applications, Hydrodynamic Nuclei Concentration (HDNC) has evolved from IPI and is applied to systems with high particle load, enabling reliable quantitative concentration analyses.[22,23] However, with both IPI and HDNC, distinguishing between different types of solid particles is challenging and often even impossible. This limitation necessitates the complementation of such approaches with an additional spectroscopic method.

1.2 Detection of microplastics in flowing water systems

For monitoring purposes, it is not sufficient to analyse MPs only in static laboratory conditions. Reliable assessment of pollution levels in natural environments requires detection and characterisation of particles directly in a water flow. Such in-flow detection provides information at higher temporal resolution and avoids potential artefacts from extensive sample preparation, storage, and transport.

Several experimental studies have recently attempted continuous in-flow detection of MPs using different physical principles. Flow-based Raman spectroscopy has been demonstrated to identify MPs in aqueous suspensions.[24,25] Glöckler *et al.*[26] combined elastic light scattering with Raman spectroscopy in a flow cuvette to both size and identify MPs within a single measurement. While these studies provide proof-of-concept results, their complexity, susceptibility to fluorescence interference, and reliance on costly spectroscopic instrumentation limit their applicability for robust *in situ* deployment.[27] Colson *et al.*[28] employed impedance spectroscopy to quantify MPs under flow conditions but did not distinguish between different plastic classes.

1.3 Fluorescence spectroscopy

Fluorescence spectroscopic methods present a promising approach to address the challenges mentioned. Previous studies have mainly relied on fluorescent dyes such as Nile Red to stain MP particles, followed by fluorescence microscopy or imaging. Maes *et al.*[29] demonstrated a rapid screening method based on Nile Red staining combined with image analysis, enabling fast quantification of MPs in environmental samples. Building on this, Prasad *et al.*[30] characterised the fluorescence spectra of Nile Red-stained MPs under different excitation conditions, showing that spectral peak positions and shapes provide valuable information for polymer identification. More recently, Ho and Feng[31] introduced a multispectral imaging approach that combines Nile Red staining with clustering algorithms to differentiate polymers based on their fluorescence response, highlighting the growing role of automated classification methods. Pizzoferrato *et al.*[32] and Bianco *et al.*[33] developed portable detectors using Nile Red staining for in-flow MP detection, while Li *et al.*[34] and Kaile *et al.*[35] applied flow cytometry to detect stained MPs down to submicron scales.

However, these methods remain technologically complex and ill-suited for robust *in situ* deployment. Nile Red staining, while simple and inexpensive, suffers from dye leaching, interference from natural organic matter and pigments, and a high risk of false positives in environmental matrices.[36,37]

In contrast to staining approaches, the intrinsic or impurity-related fluorescence of common polymers offers an alternative basis for classification. Polyethylene (PE), polypropylene (PP) and polystyrene (PS) are among the primary types of plastic found in marine pollution studies.[38] While PE and PP, as olefinic polymers, are non-fluorescent in pure form, they often contain fluorescent impurities.[39] PS is inherently fluorescent.[40] Harnessing these properties allows MPs to be classified without the need for chemical staining.

For effective *in situ* detection, a technique must be capable of simultaneously capturing the fluorescence signal of individual particles in flow and determining their size, velocity, volume and surface area, to assess contamination and potential chemical interactions *via* the integral free surface and mean volume fraction in disperse multi-phase flows.

Therefore, this study investigates the feasibility of combining fluorescence-based characterisation with particle sizing in a flowing water system, aiming to provide a simpler and more robust pathway towards *in situ* monitoring of MPs.

The focus is on reliably fluorescent particles to demonstrate *in situ* feasibility. Achieving quantitative detection of a single MP type in flow would represent an important step forward, providing a basis for subsequent extension to multi-class classification.

2 Material and methods

To analyse MPs in a flowing system, MP particles were produced and added to a liquid. The suspension was pumped into a measuring section and illuminated by a laser diode. In separate experiments, fluorescence spectra and defocused camera images were recorded to investigate the occurring phenomena.

2.1 Measuring section

The measurement setup consisted of a measuring section (Fig. 1), the centrepiece of which was a cuvette (46-F/Q/2, Starna® GmbH, Pfungstadt, Germany) with a layer thickness of 2 mm. The cuvette was held in a cuvette holder (Cuvette Holder, Qioptiq Photonics GmbH & Co. KG, Goettingen, Germany), which was installed in a LINOS Microbench cube 30 (Cube 30, Qioptiq Photonics GmbH & Co. KG, Goettingen, Germany). The cuvette was rotatably mounted, allowing either a layer thickness of 2 mm in the horizontal or vertical direction. For the measurements carried out, the cuvette was orientated horizontally, resulting in a height of 2 mm and a depth of 10 mm. This ensured the highest possible number of particles in the detection volume of the camera and the spectrometer.

The sample to be analysed was stored in a sample vessel. A tube connected the sample vessel with the measuring section and a lower-lying collecting vessel. The height difference between the sample and collecting vessels was variably adjustable, allowing the sample to flow in both directions.

The sample was directed into the measuring section and illuminated by a laser diode (PLPT5 447 KA, ams-OSRAM AG, Premstaetten, Austria). The diode emits visible laser radiation, which is potentially hazardous to the eye. All experiments were therefore conducted with appropriate protective measures (beam enclosures and laser safety eyewear) in accordance with IEC 60825 Safety of laser products. The spectrum of the laser diode (Fig. 2) recorded by a spectrometer (Avantes AvaSpec-2048x14, Avantes B.V., Apeldoorn, The Netherlands) shows a maximum at 440 nm. This deviates slightly from the centroid wavelength of 445 nm specified in the data sheet,[41] which might

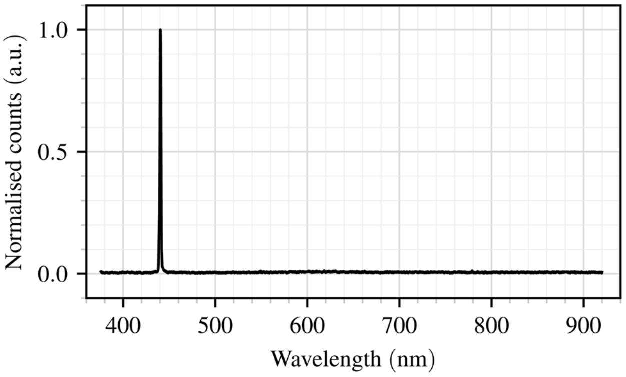

Fig. 2 Normalised spectrum of the laser diode.

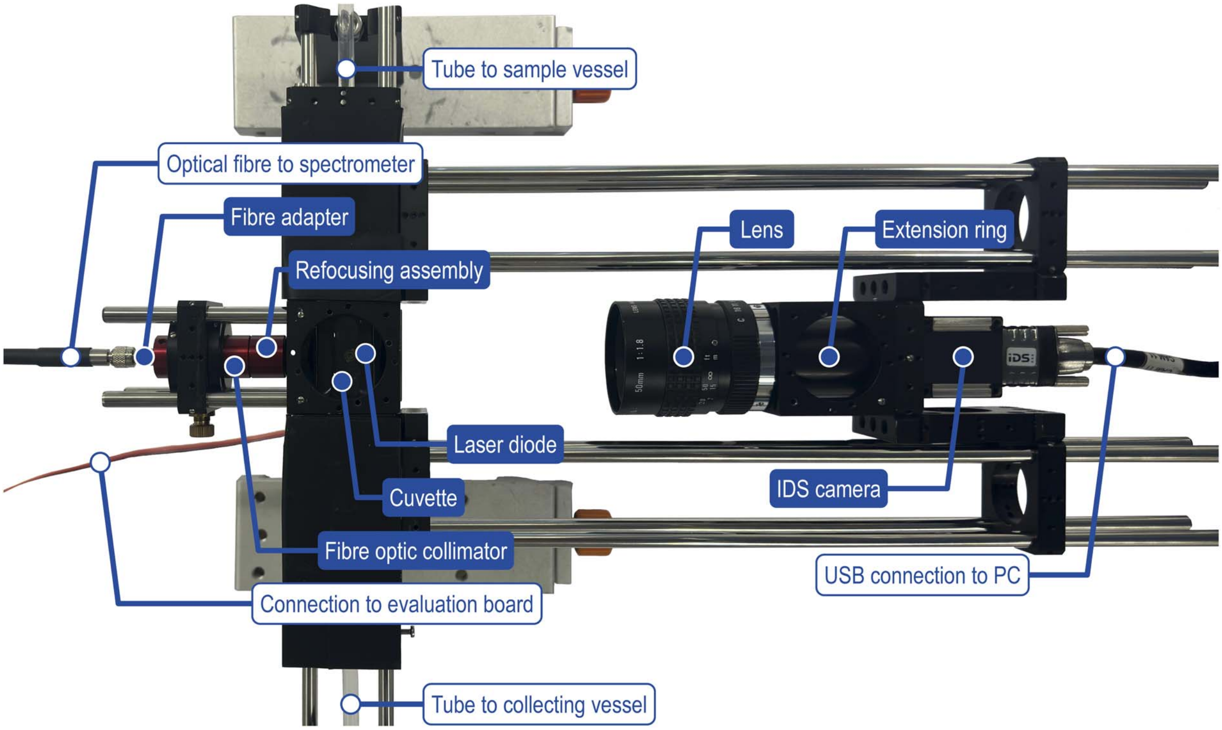

Fig. 1 Setup of the measuring section.

be attributed to a lower housing temperature of the laser diode during spectrum recording. Within the maximum range between 439 nm and 442 nm, the measured intensity counts exceeded those of the surrounding spectral regions by nearly two orders of magnitude. The output power of the laser diode was measured to be 0.3 W using a power meter (1918-C, Newport Spectra-Physics GmbH, Darmstadt, Germany). The laser light exhibited strong divergence, making it impossible to specify the exact optical power entering the measurement volume. The laser diode was driven by an evaluation board (iC-HG 3 A LASER SWITCH, iC-Haus GmbH, Bodenheim, Germany) in Automatic Current Control (ACC) mode, ensuring a constant diode current. The optical power of the laser diode could be adjusted *via* variable resistors, which were set such that the fluorescence signals of the individual samples were clearly distinguishable from the spectrometer noise. The evaluation board was supplied with 5 V from a laboratory power supply unit (HM8143, Rohde & Schwarz GmbH & Co. KG, Munich, Germany).

An IDS monochrome camera (UI-3060CP-M-GL Rev. 2, IDS Imaging Development Systems GmbH, Obersulm, Germany) was connected to a PC *via* a USB cable for video recording of the measurement volume. The camera was equipped with a fixed focal length lens (50 mm, Cosmicar Television Lens 50 mm 1 : 1.8, Cosmicar Optical Co., Ltd, Japan) and an extension ring of 40 mm. The lens was first adjusted to obtain a sharp image of the measurement volume. The camera and lens were then moved away from the measurement volume until the image became defocused, while individual particles remained recognisable. The distance between the lens mount and the centre of the cuvette was set to approximately 19 cm. This controlled defocusing is essential for IPI, as the resulting interference patterns encode information on particle size and structure. The exact degree of defocusing was empirically adjusted to optimise the visibility of the interference patterns.

Using a fibre optic collimator (10 mm Aperture UV/VIS Fiber Optic Collimator, SMA, Edmund Optics GmbH, Mainz, Germany) with a refocusing assembly (10 mm Aperture, 25 mm FL UV/VIS Fiber Refocusing Assembly, Edmund Optics GmbH, Mainz, Germany), the light scattered in the measurement volume was coupled into an optical fibre (0.22 NA UV/VIS Patchcord 400 Micron Fiber w/SMA Connector, Edmund Optics GmbH, Mainz, Germany) that connected the collimator to the spectrometer thus enabling the recording of a spectrum. The optimum insertion of the fibre adapter into the fibre optic collimator was first determined by adjusting the fibre optic collimator. To do this, the fibre was connected to the adapter and backlit. The adapter was then inserted into the collimator so that the light spot produced on a screen had a minimum diameter. The distance between the end of the refocusing unit and the screen was measured, and the collimator was placed on the measuring section so that the distance between the centre of the cell and the refocusing unit was equal to this distance. The collimator was then positioned so that the light spot in the image of the camera mounted opposite was vertically centred in the cuvette.

The camera and the collimator were positioned opposite each other, so the measurement volume was observed from the side.

2.2 Samples

As part of the test series, four PP samples with different fluorescent dyes and a PP sample without a fluorescent dye were analysed. PP was selected as the representative polymer due to its mentioned high occurrence in marine MP pollution.

To obtain fluorescent PP particles, commercially available highlighter pen caps made of intrinsically dyed PP in four colours (yellow, green, orange, and pink) (OTTO Office Textmarker Highliner Keilspitze, OTTO Office GmbH & Co. KG, Hamburg, Germany) were used. The selected colours correspond to the standard colour range of commercial highlighters and span distinct emission maxima across the visible spectrum, providing a representative set for evaluating spectroscopic discrimination while maintaining identical polymer composition. This approach yielded stable and clearly distinguishable fluorescence signals without the need for additional staining, thereby avoiding potential artefacts associated with surface treatment or dye adsorption.

The samples with fluorescent dyes were prepared from clips of the respective highlighter caps by crushing them into particles with a file and filtering them through a pointed sieve with a mesh size of 0.5 mm (Spitzsieb fein Ø 10 cm, Karl Weis u. Cie. GmbH, Murr, Germany). This resulted in a maximum particle size of about 500 µm which prevented the cuvette from clogging. The filtered particles were placed in a test tube, which was sealed with a cork stopper, preventing the ingress of foreign particles. The same was done for the sample without fluorescent dye, which was prepared from a bucket for oranges (Kaufland Dienstleistung GmbH & Co. KG, Neckarsulm, Germany) (Fig. 3).

For the particles to be analysed using the optical setup, 50 mg of the respective particle type were first weighed using a precision balance (ABT 120-5DM, KERN & SOHN GmbH, Balingen-Frommern, Germany) and placed in a laboratory screw thread bottle. As PP has a lower density than distilled water, an isopropanol–water mixture was used to lower the density of the liquid and thus allow the particles to float in the liquid. For this purpose, isopropanol (isopropanol 99.9%, Höfer Chemie GmbH, Kleinblittersdorf, Germany) with a density of 0.785 kg L^{-1} at 20 °C (ref. 42) was mixed with distilled water in

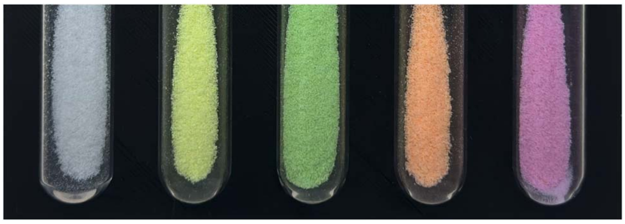

Fig. 3 Prepared samples in test tubes (from left to right): PP sample without dye and PP samples with fluorescent dyes (yellow, green, orange, pink).

a ratio of 7 to 10. The desired density of the liquid should correspond to the value of the density ρ_{PP} of PP:

Density of water:[43]

$$\rho_{H_2O} \approx 0.998 \text{ kg L}^{-1} \tag{1}$$

Density of isopropanol:

$$\rho_{iso} \approx 0.785 \text{ kg L}^{-1} \tag{2}$$

Density of PP:[44]

$$\rho_{PP} \approx 0.91 \text{ kg L}^{-1} \tag{3}$$

The total volume of the mixture should be 300 mL. Therefore, the required volume V_{iso} of isopropanol can be calculated using the densities of distilled water, isopropanol and PP:

$$V_{iso} = \frac{0.300 \text{ L}(\rho_{PP} - \rho_{H_2O})}{\rho_{iso} - \rho_{H_2O}} \approx 0.124 \text{ L} \tag{4}$$

176 mL of distilled water was then added to the calculated volume of isopropanol to obtain a total volume of 300 mL. The resulting mixture had a density of approximately 0.91 kg L^{-1}, allowing the PP particles to float. Isopropanol–water mixture was added to the laboratory screw thread bottle containing the MP sample to be analysed until the volume of the suspension was 200 mL.

The mass m_p of the particles and the volume V_s of the suspension result in the following mass concentration β:

$$\beta = \frac{m_p}{V_s} = \frac{0.050 \text{ g}}{0.200 \text{ L}} = 0.250 \text{ g L}^{-1} \tag{5}$$

The sample bottle was closed with the cap. The isopropanol–water mixture and the cap prevented unwanted biological growth and protected the sample from external influences. The suspension was then mixed with a magnetic stirrer (RSM-10HP, Phoenix Instrument GmbH, Garbsen, Germany) for one minute at the highest level to ensure a more homogeneous distribution of the particles in the sample liquid.

2.3 Spectral investigations

2.3.1 Data acquisition. During each measurement series, a sample of the prepared suspension was directed from the sample vessel through the measuring section into the collecting vessel by adjusting the vessel heights. The flow rate was controlled empirically to ensure that individual particles could be observed within the measurement volume.

Spectra were recorded with the AvaSoft-Basic software (version 8.16.1.0, Avantes B.V.) and exported to an Excel file. The integration time was set to 100 ms. The software's dark function was applied to remove background noise before each series of measurements, with the laser diode still switched off.

In the spectral region of the laser peak, the spectrometer signal reached saturation due to the high laser intensity. This was deliberately accepted in order to increase the excitation power and thereby enhance the visibility of the fluorescence phenomena.

2.3.2 Data processing. The sums of the fluorescence spectra counts recorded during each measurement series provide a quantitative measure of the fluorescence intensity of the sample under investigation. This information can be used to identify fluorescent particles in the measurement volume. Using the Python library SciPy[45] and its signal module with the find_peaks and prominences functions, the most prominent peaks in the spectrum sum were detected, indicating fluorescent particles in the measurement volume. A threshold of 0.1 was set for prominence. For each measurement series, the number of peaks with a prominence greater than 0.1 was determined, and the lowest value across all series was taken as the basis for the number of spectra to be examined. This procedure enables better comparability between the individual particle types. For the measurement series carried out, $n = 30$ proved to be a suitable number of spectra to analyse. For each fluorescent particle type, three independent measurement series were conducted to assess reproducibility and to provide separate datasets for subsequent analysis. The non-fluorescent reference sample was measured once to confirm the absence of intrinsic fluorescence in the polymer matrix.

The selected spectra were normalised to the emission maximum occurring after the laser peak ($\lambda > 460$ nm). Since the laser peak itself is not relevant for the subsequent fluorescence analysis, it was excluded from the normalisation. For this purpose, the post-laser emission maximum was set to 1 and the lowest value of the spectrum to 0, resulting in a min–max normalisation. This ensures better comparability across different samples. The mean values of the normalised spectra of each dye were then calculated for each wavelength bin and plotted together with the corresponding minimum and maximum values of the individual samples.

In addition to normalisation and averaging, characteristic spectral parameters were determined for each dye. The wavelength of the emission maximum occurring after the laser peak was calculated by identifying the global maximum of the normalised spectrum in the range ($\lambda > 460$ nm). In addition, the corresponding intensity at this maximum (I_{max}) was determined. The full width at half maximum (FWHM) was calculated by locating the wavelengths at which the spectral intensity fell to 50% of the maximum value. These two points define the left (λ_{left}) and right (λ_{right}) half-maximum boundaries, whose difference defines the FWHM.

Together, the emission maximum, its intensity (I_{max}), the FWHM, and the corresponding half-maximum boundaries provide a compact characterisation of the spectral shape of each fluorescent dye. The parameters were calculated for each sample and reported as mean values with sample variance.

2.4 Interferometric particle imaging investigations

2.4.1 Data acquisition. For IPI measurements, air bubbles were additionally introduced into the measuring section using a syringe, without selecting a specific particle type from the suspension.

A video was recorded in .avi format using the IDS peak Cockpit software (version 2.15.0.0-1803, IDS Imaging Development Systems GmbH, Obersulm, Germany). The frame rate was set to 95 s^{-1}. Before recording, the region of interest was set to 1200 px × 650 px and positioned to ensure that the cuvette was visible. The exposure time was set to 0.67 ms, thereby avoiding overexposure on average.

2.4.2 Data processing. The recorded videos were analysed after acquisition with the help of a Python script. From the defocused particle images, qualitative information was obtained on whether the object represented a solid particle or an air bubble, as well as on relative differences in particle size as indicated by the fluorescence patterns.

For this purpose, the recorded frames were manually cropped to regions containing clearly visible particles. In addition, image contrast was enhanced by a three-step preprocessing routine: (i) local contrast adjustment using CLAHE, (ii) gamma correction ($\gamma = 0.7$), and (iii) histogram stretching *via* normalisation. All procedures were implemented in Python with the OpenCV[46] library, employing the functions cv2.createCLAHE, cv2.LUT, and cv2.normalize. This ensures that interference patterns become clearly distinguishable.

3 Results and discussion

During the experimental investigations, we recorded fluorescence spectra of PP particles with different fluorescent dyes as well as of pure PP particles without any dye. For each fluorescent PP type, we conducted three independent measurement series, each comprising 30 analysed particles. A single measurement series of the pure PP sample was recorded, comprising 30 spectra to confirm the absence of intrinsic fluorescence. Additionally, we took IPI images of PP particles and air bubbles to evaluate the possibility of a differentiation between bubbles and solid particles, as well as the size determination in context of this measurement setup.

3.1 Fluorescence behaviour of pure polypropylene

For the sample with pure PP without the addition of a fluorescent dye, the counts of the recorded spectrum remain at a constant low level with no recognisable extremes (Fig. 4). This observation is consistent with the fact that PP, as an olefinic polymer, does not exhibit intrinsic fluorescence in its pure form.[39] The signal remains close to the noise level of the spectrometer, with no detectable emission peaks above background. A pronounced rise is only visible at the position of the laser peak, which, as already described in Section 2.3.1, results from the intense excitation light and the corresponding saturation of the spectrometer. This effect leads to an artificially broadened laser peak but is unrelated to fluorescence phenomena. Accordingly, the pure PP sample serves as a negative control, confirming that the fluorescence signals observed in other samples originate from the added dyes rather than from the polymer matrix itself.

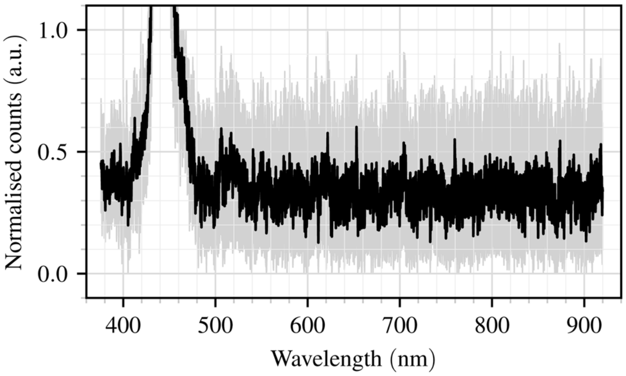

Fig. 4 Normalised mean fluorescence spectrum ($n = 30$, black line) with shaded areas indicating the minimum–maximum range of the measurement for the pure PP sample.

3.2 Fluorescence behaviour of polypropylene with different fluorescent dyes

Fig. 5 shows the normalised fluorescence spectra of the four examined PP samples with different fluorescent dyes. The mean value is shown as well as the range between the minimum and maximum values for each sample. The peaks of the excitation light are clipped due to the focus on the fluorescence phenomena. In Table 1, a summary of the spectral parameters is provided.

The spectra of yellow and green PP particles show rather broad emission bands (FWHM > 55 nm) with maxima at around 500 nm, while the spectra of orange and pink PP particles exhibit fluorescence emission with a narrower FWHM (<40 nm) and maxima at approximately 584 nm and 590 nm, respectively. These observations from the mean spectra are further supported by the distribution of $\lambda_{\max}$ values shown in the boxplots (Fig. 6). The emission peaks of yellow and green PP particles are located in a similar spectral region, while orange and pink PP particles exhibit a distinct red-shifted emission. This observation is consistent with expectations, as the spectral shifts of the emission maxima correspond to the visible colour of the respective dyes. The difference in peak position enables a clear differentiation between the two classes of PP particles (yellow/green *vs.* orange/pink) based on their fluorescence characteristics.

The boxplots further illustrate the distribution and variability of the emission maxima ($\lambda_{\max}$) within each sample and reveal important limitations. Although the median values reflect the systematic shifts between the sample classes, the Interquartile Range (IQR) of yellow lies entirely within the IQR of green, with the latter being considerably larger. Consequently, all yellow values fall within the whisker range of the green sample, making a separation between these two samples impossible. This strong overlap further supports the assumption that both materials may contain the same primary fluorescent dye. The nearly identical spectral positions and widths of the yellow and green emission bands (see Table 1) are consistent with this interpretation. The markedly lower intensity of the green sample, however, suggests that the effective dye concentration is smaller or that additional fluorescent components are present which are not efficiently excited at the

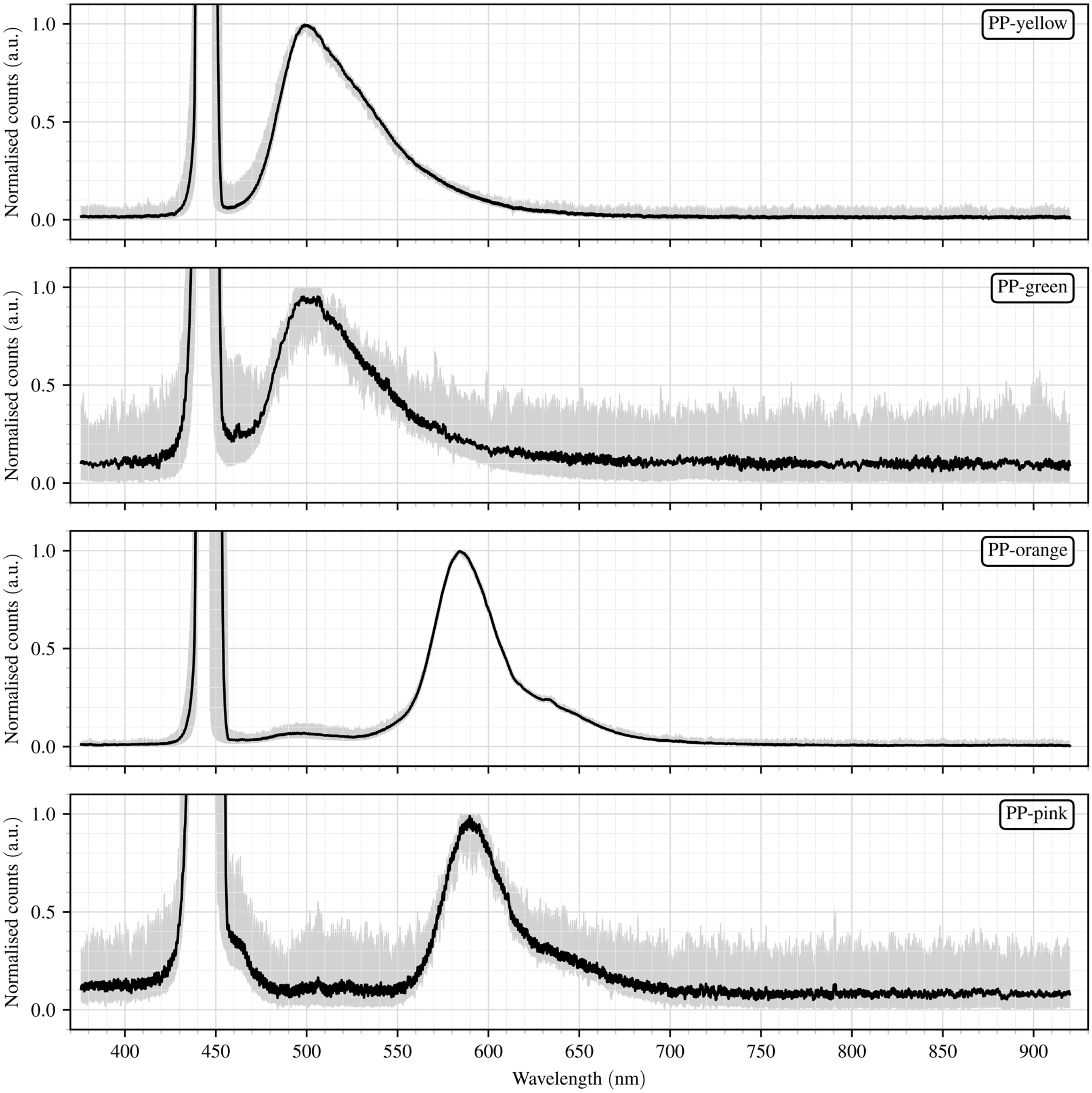

Fig. 5 Normalised mean fluorescence spectra (n = 60, black line) with shaded areas indicating the minimum–maximum range of the measurements for PP samples with different fluorescent dyes.

employed excitation wavelength of 445 nm. It is therefore plausible that the green polymer contains secondary dyes with absorption maxima at shorter wavelengths, which could become active under UV excitation. Based on this assumption, the yellow and green samples were combined into a single class in the subsequent analyses, whereas orange and pink particles

Table 1 Summary of spectral parameters of the fluorescence peaks for PP samples with different fluorescent dyes: wavelength of the emission maximum ($\lambda_{\max}$), full width at half maximum (FWHM), left and right half-maximum boundaries (λ_{left}, λ_{right}), and intensity at emission maximum ($I_{\max}$). Values are given as mean ± sample variance (n = 60)

Sample	$\lambda_{\max}$ (nm)	FWHM (nm)	λ_{left} (nm)	λ_{right} (nm)	$I_{\max}$ (a.u.)
PP-yellow	499.6 ± 1.0	58.0 ± 0.9	482.6 ± 0.9	540.6 ± 1.2	7076 ± 5169
PP-green	501.0 ± 4.0	57.3 ± 4.8	480.7 ± 1.3	538.1 ± 4.5	1131 ± 851
PP-orange	584.2 ± 0.7	39.5 ± 0.3	567.8 ± 0.4	607.3 ± 0.4	14 035 ± 11 470
PP-pink	589.8 ± 1.5	38.3 ± 1.3	573.6 ± 1.0	611.9 ± 0.7	989 ± 558

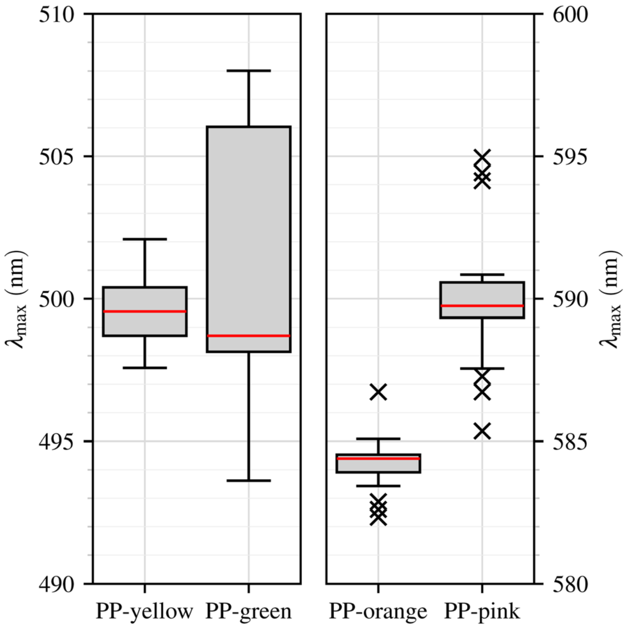

Fig. 6 Wavelengths of the emission maxima (λ_{max}) of fluorescence spectra from PP particles with different fluorescent dyes. Boxplots display the distribution of λ_{max} values, indicating median, interquartile range, whiskers, and outliers for each sample.

were retained as separate classes to evaluate their distinguishability in more detail.

For orange and pink particles, no complete overlap is observed in the boxplots. However, three outliers coincide between the two distributions, namely one orange and two pink, although all lie outside the whisker ranges of the respective other sample. This indicates that overlap occurs only at the edges of the emission distributions, while the main spectral ranges remain clearly separated.

To explore these findings in more detail, we calculated the left and right boundaries (λ_{left}, λ_{right}) of the emission peaks, providing additional information on the shape of the fluorescence peak. For the yellow and green PP particles, the left boundary lies closer to the peak than the right boundary, indicating an asymmetric peak shape with a steeper rise before the maximum than the decline afterwards. In contrast, the orange and pink PP particles show a more symmetric peak shape, with both boundaries located at comparable distances from the excitation maximum. Nevertheless, these characteristics again only allow a distinction between the two classes of PP particles (yellow/green *vs.* orange/pink) but not within the classes themselves.

The absolute intensity of the fluorescence spectra differs markedly between the PP samples (Table 1). Orange PP particles exhibit the highest intensities, followed by yellow, whereas green and pink particles show considerably lower values. However, these differences in absolute intensity are not reliable indicators for distinguishing between the samples, as they can be affected by factors such as particle size, position within the measurement volume, and orientation relative to the excitation light and the spectrometer. In addition, the sample variance is high, and the maximum intensity values of the different samples overlap substantially. This supports the conclusion that, in contrast to wavelength-based parameters, fluorescence intensity alone is not a suitable criterion for differentiating between the PP samples.

3.3 Intensity ratios as clustering parameters

Therefore, we introduce a new parameter based on the approach of Ornik *et al.*[47] to further investigate the fluorescence properties of the PP particles. The concept is to reduce the full spectral information to ratios of intensities at selected wavelengths, which can then be plotted against each other. This dimensionality reduction highlights differences between the individual samples and facilitates the formation of distinct clusters for each particle type. In our case, the spectra are represented by only one ratio R_1:

$$R_1 = \frac{I(\lambda_1)}{I(\lambda_2)} \tag{6}$$

where $I(\lambda)$ is the normalised intensity at wavelength λ. The selected wavelengths are:

$$\lambda_1 = 471.8 \text{ nm}, \tag{7}$$

$$\lambda_2 = 589.7 \text{ nm}. \tag{8}$$

The two wavelengths were determined by a grid search within the range of 460 nm–700 nm. For each candidate combination, the resulting intensity ratio R_1 was calculated for all spectra, and the separability of the three sample classes (yellow/green, orange, and pink) was evaluated based on the minimal inter-class distance in R_1 space. The configuration that maximised this minimal inter-class distance was selected as the optimal wavelength pair, ensuring the best possible discrimination between the coloured PP samples.

The selected wavelength pair also coincides with characteristic spectral regions that reflect the most pronounced differences between the emission profiles of the individual dyes. At λ_1, all spectra exhibit relatively low intensities, as this wavelength lies on the rising flank of the yellow and green emission bands and still within the low-intensity region of the orange and pink spectra. At λ_2, the pink spectra reach their emission maximum, while the orange spectra remain close to it, whereas the yellow and green emissions have already decreased substantially.

The distribution of the R_1 values for the different PP samples is shown in Fig. 7 (train), illustrating the resulting class separation for both the training and the test data sets. Using this approach, we can effectively differentiate between the various PP samples based on their fluorescence characteristics. Yellow/green PP particles correspond to low R_1 values (<1.2), pink particles exhibit intermediate values between 3.3 and 10.4, and orange particles show high values (>15.8).

These distinct R_1 ranges demonstrate that even a single intensity ratio captures the most pronounced spectral differences between the samples, providing a reliable and efficient basis for their classification.

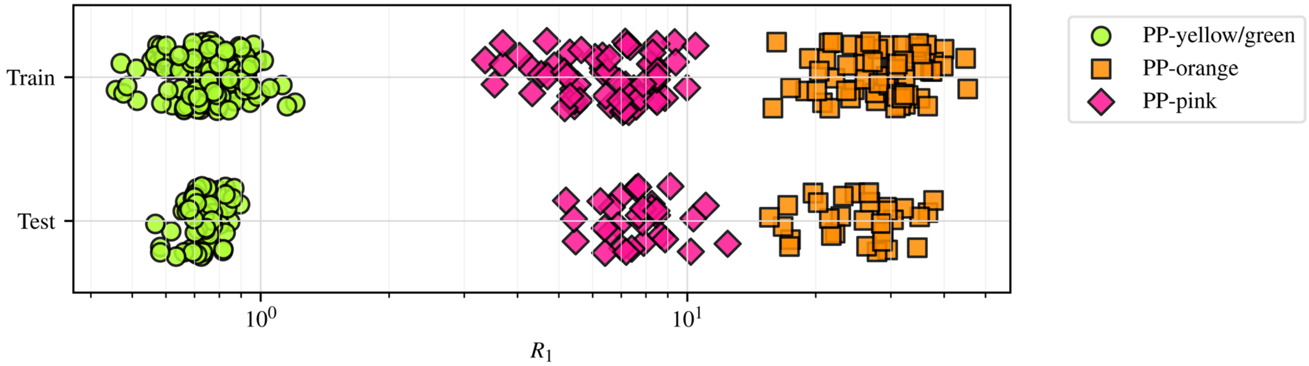

Fig. 7 Train and test values of R_1 for PP samples with different fluorescent dyes. Each point corresponds to one particle; colours denote fluorescent dyes (yellow/green, orange, pink). The upper row shows the training data, while the lower row displays the corresponding test data.

3.4 Numerical clustering

To further sharpen class separation among the PP samples, we adopted a two-stage dimensionality-reduction pipeline. Since the spectra for orange and pink particles are highly correlated, a purely class-agnostic approach such as Principal Component Analysis (PCA) is unlikely to yield feature combinations that optimally separate the classes. This limitation arises because PCA maximises total variance without reference to class labels.[48] The pipeline couples unsupervised PCA with a supervised discriminant projection. While this approach is less interpretable than clustering *via* intensity ratios, it is well established[49] and does lead to better separation of the PP classes.

The high dimensionality of each spectrum (2048 bins) renders direct supervised modelling prone to overfitting and ill-conditioned covariance estimates. We therefore first applied class-agnostic PCA to obtain a compact representation. Retaining the first 17 principal components preserved the dominant variance of the data while attenuating measurement noise and substantially reducing the parameter burden of the subsequent model.

On these principal components, we then fitted a Linear Discriminant Analysis (LDA), which explicitly seeks linear combinations that maximise between-class separation relative to within-class variance.[50] Importantly, performing PCA before LDA regularises the LDA covariance estimate and mitigates overfitting. Moreover, the class-agnostic nature of PCA prevents label leakage and preserves a neutral preprocessing step.[49]

In our three-class setting, LDA yields at most two linear discriminants. Accordingly, LD_1 and LD_2 together account for 100% of the between-class variance, with LD_1 explaining 75% and LD_2 the remaining 25%. These two axes are sufficient to clearly separate the PP classes, as shown in Fig. 8a. Table 2 reports the mean silhouette coefficient (SC) for both the intensity-ratio method and the numerical approach, underscoring the superior performance of the latter. SCs were computed using the silhouette_score function from scikit-learn,[51] with Euclidean distance and the ground-truth PP class labels. The SC quantifies clustering quality by jointly assessing intra-class cohesion and inter-class separation. Values range from −1 (misassignment) to 1 (compact, well-separated clusters).

Compared to the intensity-ratio baseline, the numerical clustering approach yields higher SCs for the orange and pink PP classes as well as for the overall dataset (see Table 2). The most pronounced improvement is observed for the pink particles (0.614 → 0.841), indicating a substantially more compact and homogeneous cluster structure. The orange class also benefits from a noticeable increase (0.607 → 0.801), reflecting reduced overlap with neighbouring classes. In contrast, the yellow/green particles exhibit an appreciable decrease (0.972 → 0.800), which is likely due to their already near-ideal separation in the intensity-ratio space. Overall, the numerical approach yields a slightly higher mean SC (0.810 *vs.* 0.791) than the intensity-ratio method, indicating more consistent and well-balanced class separation across all PP classes.

While the higher SCs demonstrate more compact and better-separated clusters in our dataset, this internal validity index alone does not guarantee superior generalisation to unseen data. The SC is computed on the same samples used to construct the discriminant space and therefore reflects within-sample structure rather than predictive performance.

3.5 Validation of clustering approaches

To assess the generalisation capability of the clustering strategies, we employed a supervised classification framework. The previously analysed spectra served as the training set, while an additional measurement series provided unseen test data. In this series, 30 spectra were recorded for each of the original colour classes, resulting in a total of 120 test spectra. The yellow and green particles were again treated as a single combined class, yielding 60 test spectra for the yellow/green class and 30 each for the orange and pink classes.

The validation compared two feature-extraction pipelines that differ fundamentally in their level of abstraction. The intensity-ratio approach condenses the spectral information into a single parameter R_1 derived from selected wavelength intensities, providing an interpretable, physically motivated descriptor. The numerical clustering approach, in contrast, uses PCA to reduce dimensionality and suppress noise, followed by LDA to obtain discriminant coordinates optimised for class separation.

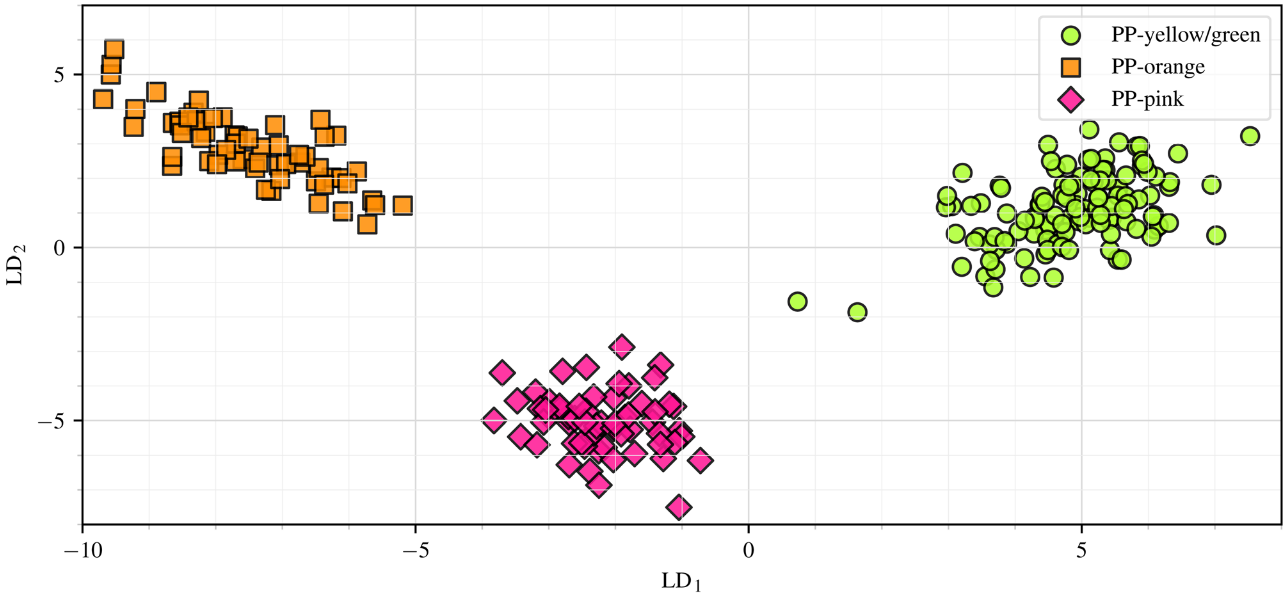

(a) Training dataset. Clustering of fluorescent PP particles projected onto the first two linear discriminants (LD_1 and LD_2).

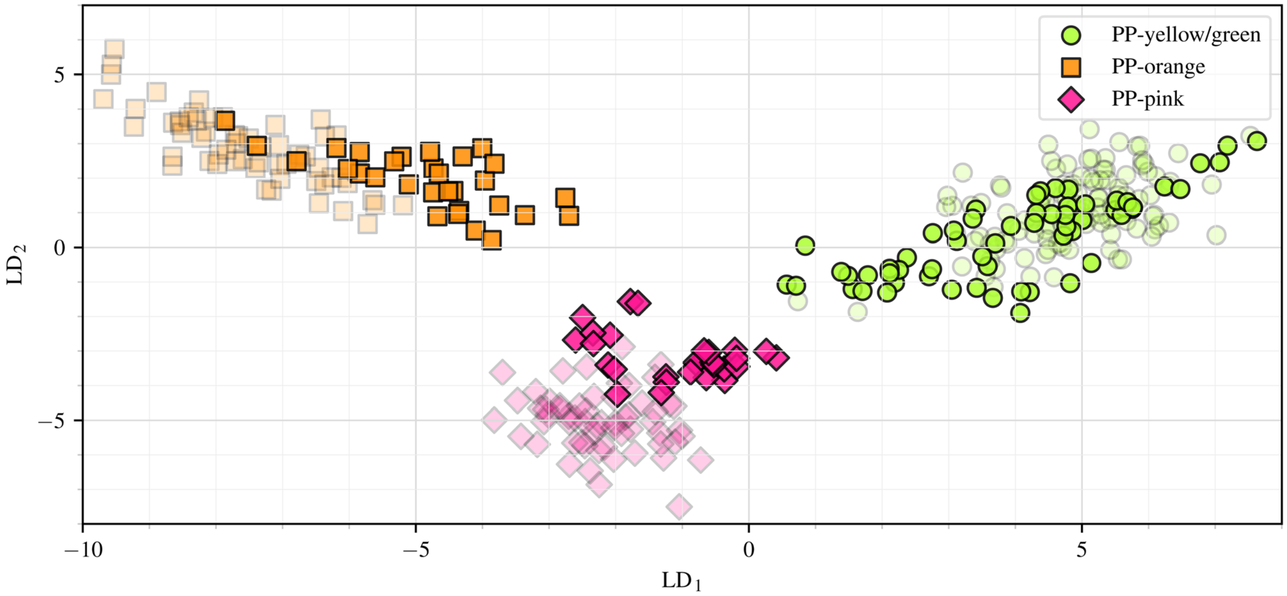

(b) Test dataset. Validation of the clustering performance on an independent measurement series. The training data are shown faintly in the background for reference.

Fig. 8 Numerical clustering and validation of fluorescent PP particle classes. Scatter plots of the PP samples projected onto the first two linear discriminants (LD_1 *vs.* LD_2) computed from PCA scores (17 principal components). Each point represents one particle; colours indicate PP subclasses (yellow/green, orange, pink). Subfigure (a) shows the clustering obtained from the training data, while subfigure (b) displays the corresponding validation using the test dataset.

In both cases, the extracted features were classified using a k-nearest neighbour algorithm ($k = 5$, Euclidean distance). This ensured methodological consistency, as LDA was used exclusively for feature extraction rather than classification. The models were trained on the original dataset, and the learned transformations were subsequently applied to the independent measurement series without further adjustment.

To further verify robustness, a stratified n_{CV}-fold cross-validation ($n_{\mathrm{CV}} = 10$) was performed using the complete dataset, including both the original training set and the independent test data. This procedure maintained the original class ratios within each fold and ensured that every sample was used once for testing and nine times for training. For each split, the same feature representations and classification settings were applied, and the resulting performance metrics were averaged across all folds. The cross-validation results were consistent with those of the independent test evaluation, confirming the reproducibility and stability of both clustering approaches.

Table 2 Mean silhouette coefficients for the intensity-ratio method (SC_I) and the numerical clustering approach (SC_N) for each PP class and overall. Values range from −1 to 1 where higher values indicate better cluster separation and compactness

Class	SC_I	SC_N
PP-yellow/green	0.972	0.800
PP-orange	0.607	0.801
PP-pink	0.614	0.841
Overall	0.791	0.810

Performance was evaluated in terms of overall accuracy, macro-averaged precision, recall, and F1-score, complemented by the multi-class ROC-AUC.

The independent validation results are shown in Fig. 7 (test) and Fig. 8b. Both visualisations demonstrate consistent class separation between the training and the independent test data, while the quantitative metrics in Table 3 confirm comparable classification performance across the two approaches. The stratified n_{CV}-fold cross-validation ($n_{CV} = 10$) produced identical results across all folds, further supporting the robustness of both methods. For both the independent test data and the cross-validation, all evaluated metrics reached a value of 1.0, indicating perfect agreement between predicted and true class labels.

This result establishes a crucial performance baseline, demonstrating that both approaches achieve accurate and reproducible class separation under these controlled conditions. This flawless classification of pristine, commercially-sourced particles confirms the high inherent separability of the selected fluorescent dyes, validating the fundamental measurement concept by proving their spectral features are stable and algorithmically separable within this sample set. This successful validation is a necessary prerequisite for testing on more complex datasets. However, applying this baseline to real-world environmental samples (which may be weathered, bio-fouled, or from different batches) remains a key challenge for future work.

3.6 Solid-bubble-discrimination using interferometric particle imaging

Initial IPI images were recorded to confirm the feasibility of differentiating between bubbles and solid particles, as well as to assess the potential for particle size determination within this measurement setup. An example of defocused images of PP particles and air bubbles is shown in Fig. 9. These first images demonstrate the distinction between air bubbles and PP particles based on their interference patterns. As described by Albrecht *et al.*,[17] solid particles such as PP exhibit a speckle pattern, whereas (air) bubbles display interference fringes. Moreover, particle size can be inferred from the dimensions of these structures: smaller solid particles produce larger speckles, while larger solids show smaller speckles.[20,21,52] In contrast, smaller bubbles exhibit fewer interference fringes, whereas larger bubbles show a higher number of fringes.[17–19]

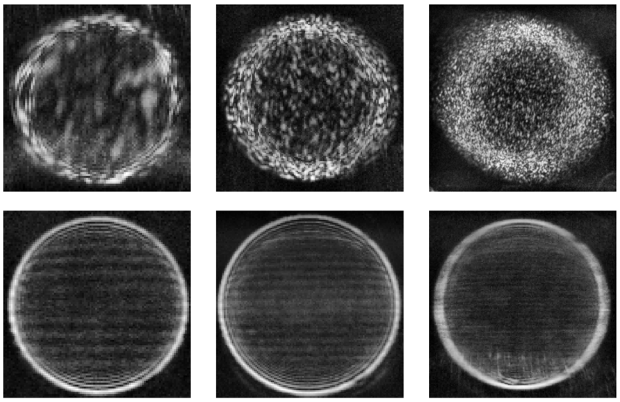

Fig. 9 Defocused images of PP particles (top) and air bubbles (bottom). Particle size increases from left to right, as indicated by the change in fringe and speckle structure rather than by the apparent image diameter. Images were cropped to the particle and contrast enhanced to improve clarity.

To investigate the effect of particle size on the fluorescence response and to demonstrate preliminary synchronisation between imaging and spectroscopy, selected orange PP particles were positioned within the measurement volume and recorded manually in both channels. For each particle, an IPI image and the corresponding fluorescence spectrum were acquired under identical optical conditions. Fig. 10 displays the IPI images together with the corresponding spectra for three particles of different sizes. Particle size increases from top to bottom, which is reflected by finer speckle structures in the IPI images and increased fluorescence intensities in the spectra. These results qualitatively confirm that the fluorescence signal scales with the effective scattering and emitting volume of the particle, while the spectral shape remains characteristic for the dye type, except for minor distortions caused by noise at low signal levels.

Table 3 Scoring metrics for intensity-ratio (IR) and numerical (*N*) approaches based on the independent test dataset (T) and stratified n_{CV}-fold cross-validation (CV, $n_{CV} = 10$). All folds in the CV yielded identical scores

Metric	IR_T	N_T	IR_{CV}	N_{CV}
Accuracy	1.0	1.0	1.0	1.0
Precision	1.0	1.0	1.0	1.0
Recall	1.0	1.0	1.0	1.0
F1-score	1.0	1.0	1.0	1.0
ROC-AUC	1.0	1.0	1.0	1.0

3.7 Challenges and limitations

Several challenges and limitations were encountered during the measurements that could affect the reliability and accuracy of the results. One major issue was the variability in particle size, morphology, and orientation within the measurement volume. These parameters primarily influenced the detected fluorescence intensity: larger or more favourably oriented particles yielded stronger signals, while smaller or unfavourably aligned ones produced weaker emissions. The influence of particle size on fluorescence intensity was qualitatively assessed through

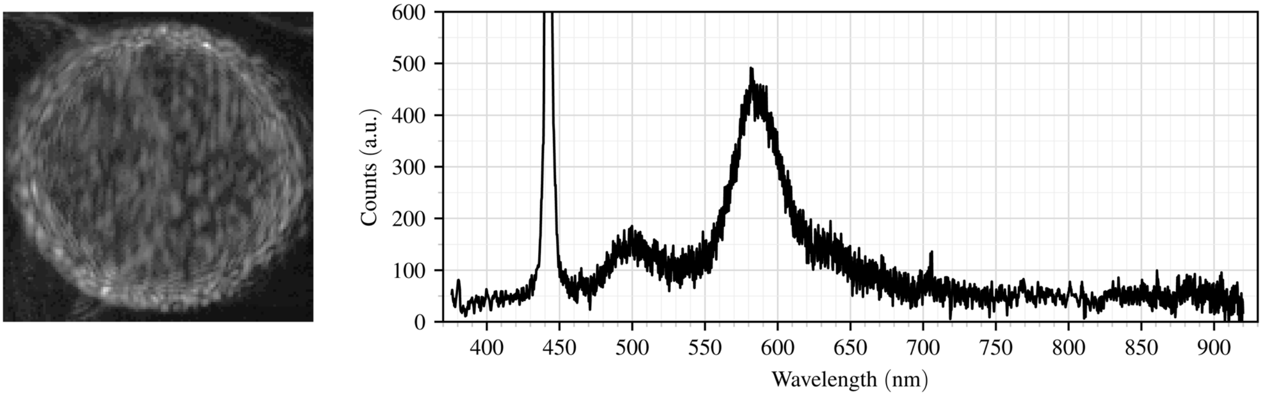

(a) Small PP particle with low fluorescence intensity.

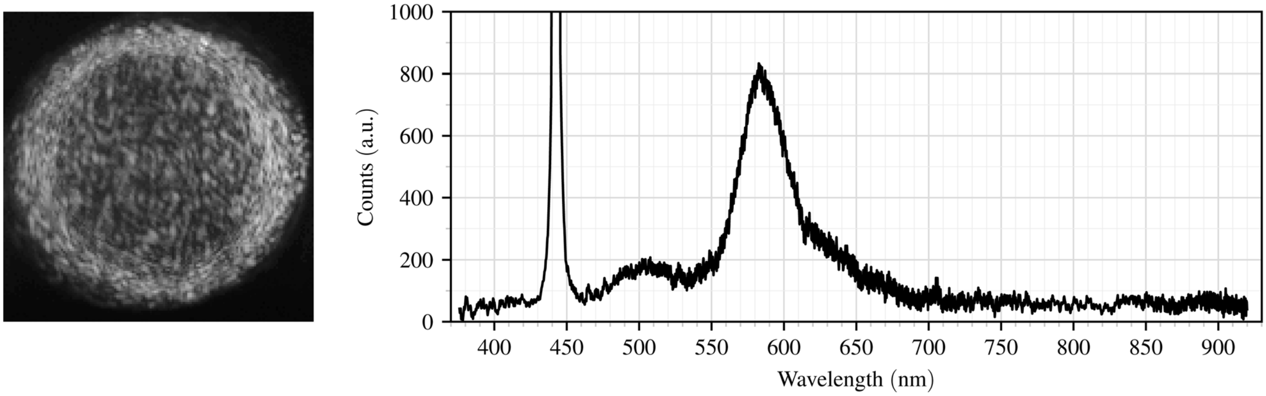

(b) Medium-sized PP particle with intermediate fluorescence intensity.

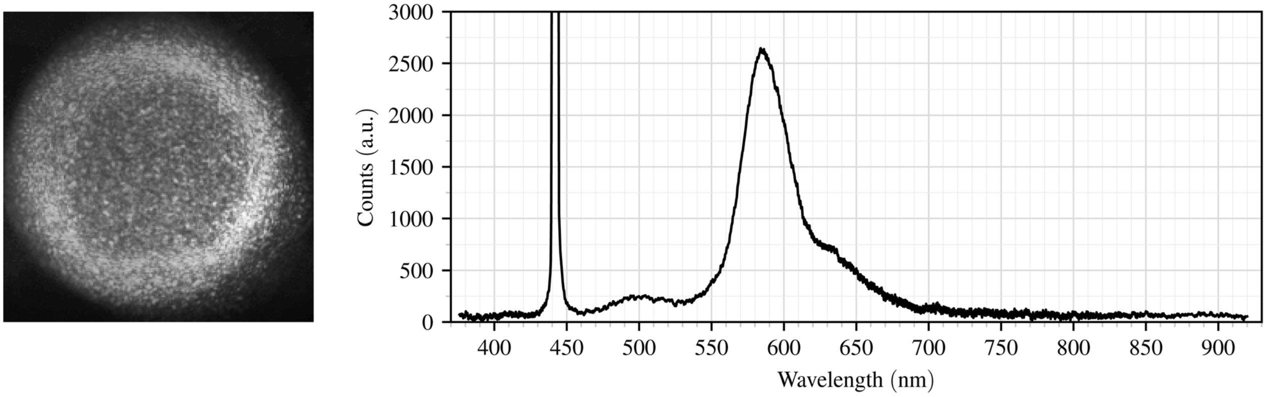

(c) Large PP particle with highest fluorescence intensity.

Fig. 10 Manually synchronised acquisition of IPI images (left) and corresponding fluorescence spectra (right) for individual orange PP particles of increasing size from top to bottom. The comparison highlights how particle morphology and fluorescence emission vary systematically with size, illustrating the qualitative correlation between speckle structure and fluorescence intensity.

manually synchronised IPI-spectroscopy measurements. These tests confirmed a general correlation between particle size and emission strength, yet a quantitative calibration linking IPI-derived size metrics to absolute fluorescence intensity has not yet been established. At this stage, the evaluation therefore permits only the comparison of relative size differences between particles. Future efforts will focus on developing calibration procedures and assessing both the accuracy of size determination and the robustness of particle differentiation under realistic marine conditions. This manually synchronised acquisition thus represents an intermediate step toward fully coupled IPI-fluorescence measurements, which will be implemented using a common trigger system in forthcoming experiments.

While weak fluorescence of tiny particles was not the focus of this study, weakly or non-fluorescent MPs remain an important challenge for future investigations. To enhance excitation efficiency and signal strength, upcoming experiments will investigate both a broadband light source covering the characteristic absorption bands of different polymers and a high-power UV laser providing narrow-band, high-energy radiation at short wavelengths. These approaches are expected to excite fluorescence in a wider range of materials and to yield stronger emission signals even for tiny particles. In parallel, a custom-built spectrometer with enhanced sensitivity in the UV range (230 nm–400 nm) and an improved optical setup with spectral filtering of excitation and stray light are being developed to enable the detection of weak fluorescence with higher precision. As the present study focused on fluorescence-based characterisation rather than absolute intensity analysis, these variations were considered acceptable for this proof-of-concept demonstration. Nevertheless, the potential influence of particle size and morphology on classification accuracy should be systematically evaluated in future work.

The saturated laser peak, while necessary to enhance fluorescence visibility, introduced artefacts that obscured nearby spectral features, and background noise further complicated accurate spectral acquisition. Data selection presented another challenge, as the inclusion of spectra was determined by the prominence of the spectral sum peaks. Broad peaks were excluded to avoid misinterpretation, though this selection may have introduced bias. Overlapping signals from multiple particles within the measurement volume also represent a challenge, which can be mitigated by the HDNC technique using a narrow laser beam.[22,23] The limited number of spectra analysed for each sample ($n = 60$) may not fully capture the variability within each class. This limitation has been partly addressed by acquiring an independent test dataset with 30 additional spectra per colour class, confirming the generalisation of both feature-extraction approaches. Increasing the dataset in future studies will further strengthen the robustness and statistical validity of the results.

Additional methodological constraints were also identified. Pure PP particles were used as a negative control to confirm that fluorescence signals originated from the dyes rather than the polymer matrix. However, since pure PP showed no intrinsic fluorescence, potential background signals from impurities could not be assessed, although such effects may be relevant in environmental samples. Furthermore, the exact nature of the incorporated dyes in the coloured particles was unknown. These dyes may have influenced the observed fluorescence intensities, particularly as the green and pink PP particles consistently showed lower intensity values. At the same time, such differences could equally be explained by smaller particle sizes. The combined use of fluorescence spectroscopy and IPI offers a promising route to disentangle these effects by directly correlating spectral features with particle dimensions. The investigation was also restricted to PP. Other polymers such as PE or PS were not considered but may behave differently. Furthermore, the use of a single excitation wavelength (445 nm) limited the ability to fully characterise the dyes, as some may have excitation maxima at other wavelengths.

Furthermore, while the expanded dataset and subsequent validation confirmed the high classification accuracy of the models, it is crucial to interpret this result within the context of the sample set. The particles used for training and testing were pristine, homogeneous fragments sourced directly from new commercial products. This represents an ideal best-case scenario, chosen to demonstrate the fundamental feasibility of the fluorescence-based approach. In contrast, environmental MP will exhibit far greater variability due to weathering, fragmentation, and biofouling, which can introduce spectral artefacts or alter emission characteristics. Moreover, the current model was not challenged with other potentially fluorescent materials (*e.g.* different polymers or natural organic matter) that are expected to occur *in situ*. Therefore, while the high accuracy achieved highlights the potential of the method, the model's robustness and its ability to correctly classify or reject unknown signals within a complex environmental matrix remain to be rigorously assessed.

Finally, several experimental limitations should be acknowledged. Prolonged illumination may have caused photobleaching, reducing fluorescence intensity over time. Moreover, the absence of an automated synchronisation mechanism between IPI imaging and spectrometer readings prevented a fully coupled, per-particle correlation of size and fluorescence properties. The current setup demonstrated manual synchronisation for selected particles, marking an intermediate step toward a fully integrated system. A hardware-based triggering unit for simultaneous acquisition is currently under development and will be implemented in future experiments. In addition, no active control of the sample flow was implemented in the present setup, as constant flow conditions were not critical for the objectives of this proof-of-concept study. Future implementations will include a pump-driven circulation system with a feedback loop to monitor and stabilise the volumetric flow rate.

Addressing these challenges in future work will be crucial to refine the methodology and improve the accuracy, robustness, and generalisability of MP detection and classification using fluorescence spectroscopy and IPI.

4 Conclusions

The developed setup demonstrates the ability to differentiate between fluorescent and non-fluorescent particles using clustering methods. This allows the detection of fluorescent MP particles in a flowing water system. In addition, IPI allowed solid particles to be distinguished from air bubbles and provided qualitative information on particle size, highlighting its potential as a complementary tool for particle characterisation. However, weak fluorescence signals from small particles remain a limitation for reliable detection.

Building on these findings and limitations, future work will focus on excitation with shorter wavelengths to induce fluorescence in a wider range of MP and their impurities. This will enhance the differentiation of MP from other marine materials such as sand, algae, or sediment, facilitating their classification in an *in situ* solution. Moreover, particle concentrations and fluxes could be quantified in combination with counting particle measurement techniques, *e.g.* defocussing multidimensional particle sizing.[22,23] Additionally, trigger signals can be used to synchronise the measurement of the particle size and the fluorescence spectrum, allowing for a more detailed analysis of the particles.

Together, these advances will help refine the methodology and contribute to a more robust framework for *in situ* detection and classification of MP in aquatic environments.

Author contributions

Nico Merck: conceptualisation, formal analysis, methodology, investigation, software, writing – original draft, visualisation. Jonas Otto: formal analysis, software, writing – original draft. Martin Schaeper: conceptualisation, supervision, writing – review & editing. Nils Damaschke: conceptualisation, supervision, writing – review & editing.

Conflicts of interest

There are no conflicts to declare.

Data availability

All data supporting the findings of this study are openly available in the repository at **https://doi.org/10.5281/zenodo.17431128**.[53] The repository contains the developed analysis code (version 2.0.0), the complete set of fluorescence spectra from all measurement series (including those not analysed in this manuscript), and additional defocused images from the IPI experiments.

Acknowledgements

Part of this work has been presented at the International Conference on Microplastics, Nanoplastics & Human Health in Dublin in 2024.

References

1 J. G. B. Derraik, *Mar. Pollut. Bull.*, 2002, **44**, 842–852.
2 C. Corinaldesi, S. Canensi, A. Dell'Anno, M. Tangherlini, I. Di Capua, S. Varrella, T. J. Willis, C. Cerrano and R. Danovaro, *Commun. Biol.*, 2021, **4**, 431.
3 A. Witczak, L. Przedpełska, K. Pokorska-Niewiada and J. Cybulski, *Toxics*, 2024, **12**, 571.
4 R. Mascarenhas, R. Santos and D. Zeppelini, *Mar. Pollut. Bull.*, 2004, **49**, 354–355.
5 F. Murray and P. R. Cowie, *Mar. Pollut. Bull.*, 2011, **62**, 1207–1217.
6 M. N. Issac and B. Kandasubramanian, *Environ. Sci. Pollut. Res.*, 2021, **28**, 19544–19562.
7 L. Van Cauwenberghe and C. R. Janssen, *Environ. Pollut.*, 2014, **193**, 65–70.
8 D. Neves, P. Sobral, J. L. Ferreira and T. Pereira, *Mar. Pollut. Bull.*, 2015, **101**, 119–126.
9 E. Winiarska, M. Jutel and M. Zemelka-Wiacek, *Environ. Res.*, 2024, **251**, 118535.
10 M. R. Gregory, *Mar. Pollut. Bull.*, 1996, **32**, 867–871.
11 M. A. Browne, T. Galloway and R. Thompson, *Integr. Environ. Assess. Manage.*, 2007, **3**, 559–561.
12 L. S. Fendall and M. A. Sewell, *Mar. Pollut. Bull.*, 2009, **58**, 1225–1228.
13 M. A. Browne, P. Crump, S. J. Niven, E. Teuten, A. Tonkin, T. Galloway and R. Thompson, *Environ. Sci. Technol.*, 2011, **45**, 9175–9179.
14 F. Dubaish and G. Liebezeit, *Water, Air, Soil Pollut.*, 2013, **224**, 1352.
15 R. C. Thompson, Y. Olsen, R. P. Mitchell, A. Davis, S. J. Rowland, A. W. G. John, D. McGonigle and A. E. Russell, *Science*, 2004, **304**, 838.
16 V. Hidalgo-Ruz, L. Gutow, R. C. Thompson and M. Thiel, *Environ. Sci. Technol.*, 2012, **46**, 3060–3075.
17 H.-E. Albrecht, N. Damaschke, M. Borys and C. Tropea, *Laser Doppler and Phase Doppler Measurement Techniques*, Springer Science & Business Media, 2002.
18 M. Maeda, Y. Akasaka and T. Kawaguchi, *Exp. Fluids*, 2002, **33**, 125–134.
19 N. Damaschke, H. Nobach, T. I. Nonn, N. Semidetnov and C. Tropea, *Exp. Fluids*, 2005, **39**, 336–350.
20 Z. Ulanowski, E. Hirst, P. H. Kaye and R. Greenaway, *J. Quant. Spectrosc. Radiat. Transfer*, 2012, **113**, 2457–2464.
21 M. Brunel, H. Shen, S. Coëtmellec, G. Gréhan and T. Delobel, *Int. J. Opt.*, 2014, **2014**, 143904.
22 E. Ebert, A. Kleinwächter, R. Kostbade and N. Damaschke, *17th International Symposium on Applications of Laser Techniques to Fluid Mechanics*, Lisbon, 2014, pp. 07–10.
23 E. Ebert, PhD thesis, Universität Rostock, 2015.
24 A.-K. Kniggendorf, C. Wetzel and B. Roth, *Sensors*, 2019, **19**, 1839.
25 E. I. Paruli, A. De Lavigne Sainte-Suzanne, M. Debeaumont, L. Thomas, R. Courson, L. Challier, M. El Rakwe and E. Prado, *RSC Adv.*, 2025, **15**, 33139–33150.
26 F. Glöckler, F. Foschum and A. Kienle, *Sensors*, 2023, **23**, 781.
27 S. Primpke, S. H. Christiansen, W. Cowger, H. De Frond, A. Deshpande, M. Fischer, E. B. Holland, M. Meyns, B. A. O'Donnell, B. E. Ossmann, M. Pittroff, G. Sarau, B. M. Scholz-Böttcher and K. J. Wiggin, *Appl. Spectrosc.*, 2020, **74**, 1012–1047.
28 B. C. Colson and A. P. M. Michel, *ACS Sens.*, 2021, **6**, 238–244.
29 T. Maes, R. Jessop, N. Wellner, K. Haupt and A. G. Mayes, *Sci. Rep.*, 2017, **7**, 44501.
30 S. Prasad, A. Bennett and M. Triantafyllou, *J. Mar. Sci. Eng.*, 2024, **12**, 1403.
31 D. Ho, P. Prabhakar, K. G. Karthikeyan and H. Feng, *J. Environ. Chem. Eng.*, 2025, **13**, 117944.
32 R. Pizzoferrato, Y. Li and E. Nicolai, *Photonics*, 2023, **10**, 508.
33 A. Bianco, L. Carena, N. Peitsaro, F. Sordello, D. Vione and M. Passananti, *Environ. Chem. Lett.*, 2023, **21**, 647–653.

34 J. Li, F. Huang, G. Zhang, Z. Zhang and X. Zhang, *Front. Chem.*, 2023, **11**, 1201734.

35 N. Kaile, M. Lindivat, J. Elio, G. Thuestad, Q. G. Crowley and I. A. Hoell, *Front. Mar. Sci.*, 2020, **7**, 1–12.

36 F. Ribeiro, A. C. Duarte and J. P. da Costa, *TrAC, Trends Anal. Chem.*, 2024, **172**, 117555.

37 J. S. Randhawa, *Bull. Natl. Res. Cent.*, 2023, **47**, 174.

38 A. E. Schwarz, T. N. Ligthart, E. Boukris and T. van Harmelen, *Mar. Pollut. Bull.*, 2019, **143**, 92–100.

39 S. R. Ahmad, *J. Phys. D: Appl. Phys.*, 1983, **16**, L137.

40 L. J. Basile, *J. Chem. Phys.*, 1962, **36**, 2204–2210.

41 ams-OSRAM AG, *PLPT5 447KA, Version 1.0*, 2022, https://look.ams-osram.com/m/7506b69862d5a94e/original/PLPT5-447KA.pdf.

42 Louisiana State University, Isopropyl Alcohol Solvent Properties, 2024, https://macro.lsu.edu/howto/solvents/ipa.htm, last accessed 17th September 2024.

43 M. Tanaka, G. Girard, R. Davis, A. Peuto and N. Bignell, *Metrologia*, 2001, **38**, 301.

44 Kern GmbH, Polypropylen Copolymer schlagzäh (PP-C HI), 2024, https://www.kern.de/de/technisches-datenblatt/polypropylen-pp-c-hi?n=1504_1, last accessed 17th September 2024.

45 P. Virtanen, R. Gommers, T. E. Oliphant, M. Haberland, T. Reddy, D. Cournapeau, E. Burovski, P. Peterson, W. Weckesser, J. Bright, S. J. van der Walt, M. Brett, J. Wilson, K. J. Millman, N. Mayorov, A. R. J. Nelson, E. Jones, R. Kern, E. Larson, C. J. Carey, İ. Polat, Y. Feng, E. W. Moore, J. VanderPlas, D. Laxalde, J. Perktold, R. Cimrman, I. Henriksen, E. A. Quintero, C. R. Harris, A. M. Archibald, A. H. Ribeiro, F. Pedregosa, P. van Mulbregt and SciPy 1.0 Contributors, *Nat. Methods*, 2020, **17**, 261–272.

46 G. Bradski, *Dr. Dobb's J. Softw Tools*, 2000.

47 J. Ornik, S. Sommer, S. Gies, M. Weber, C. Lott, J. C. Balzer and M. Koch, *Appl. Phys. B*, 2019, **126**, 15.

48 I. T. Jolliffe and J. Cadima, *Philos. Trans. R. Soc. London, Ser. A*, 2016, **374**, 20150202.

49 P. Belhumeur, J. Hespanha and D. Kriegman, *IEEE Trans. Pattern Anal. Mach. Intell.*, 1997, **19**, 711–720.

50 R. A. Fisher, *Ann. Eugen.*, 1936, **7**, 179–188.

51 F. Pedregosa, G. Varoquaux, A. Gramfort, V. Michel, B. Thirion, O. Grisel, M. Blondel, P. Prettenhofer, R. Weiss, V. Dubourg, J. Vanderplas, A. Passos, D. Cournapeau, M. Brucher, M. Perrot and E. Duchesnay, *J. Mach. Learn. Res.*, 2011, **12**, 2825–2830.

52 T. Steinmetz, E. Ebert and N. Damaschke, *12th International Conference on Laser-Light and Interactions with Particles*, College Station, 2018, pp. 1–3.

53 N. Merck and J. Otto, *Nico-Merck/fluorescent-microplastic-detection: Extended Proof-Of-Concept with Additional Datasets and Validation Framework*, 2025, doi: DOI: 10.5281/zenodo.17431128.